The effect of deformation bands on simulated fluid flow within fault-propagation fold trap types: Lessons from the San Rafael monocline, Utah

Luisa F. Zuluaga, Atle Rotevatn, Eirik Keilegavlen, and Haakon Fossen

ABSTRACT

Porous siliciclastic reservoirs are known to contain structural heterogeneities such as deformation bands, which fall below current seismic resolution and which generally cannot be explicitly represented in reservoir models because of the prohibitively high computational cost. In this study, we built a reservoir model to evaluate fluid flow across a contractionally folded unit containing deformation bands (the Navajo Sandstone in the San Rafael Reef monocline, Utah). Using field data, geometric relationships, and auxiliary computational techniques, we upscale deformation bands to capture flow effects in the large-scale structure, running simulations with variable scenarios of permeability contrast between host rock and deformation bands. Our simulations show that pervasive deformation band arrays (such as the ones present in the monocline) have effects when the contrast of permeability between them and the host rock is of at least three orders of magnitude, delaying water breakthrough and enhancing sweep; in long-term production, this results in larger final produced volumes and higher total recovery. Because of the wide range of deformation band permeabilities used in this study, our findings can be of importance for the prediction of flow and optimization of production strategies in comparable traps and reservoirs. Additionally, auxiliary computational techniques and geometric relationships such as the ones presented in this study can significantly improve the incorporation of small-scale features with strong scale gap into conventional sized reservoirs.

Manuscript received August 22, 2014; provisional acceptance July 9, 2015; revised manuscript received October 5, 2015; revised manuscript provisional acceptance January 6, 2016; 2nd revised manuscript received February 3, 2016; final acceptance April 15, 2016.
DOI:10.1306/04151614153

AUTHORS

Luisa F. Zuluaga ~ *Centre for Integrated Petroleum Research, Uni Research, Allégaten 41, 5007 Bergen, Norway; Department of Earth Science, University of Bergen, Allégaten 41, 5007 Bergen, Norway; luisa.zuluaga@uni.no*

Luisa F. Zuluaga obtained a Ph.D. in structural geology from the University of Bergen (2015), an M.Sc. in petroleum geosciences from Institut Français du Pétrole School (2009), and a geology diploma from the National University of Colombia (2007). She has worked a variety of exploration assignments in onshore and offshore Colombia. Her current interests focus on structural characterization and tectonic controls of reservoir rocks and effect on fluid flow using exhumed analogs.

Atle Rotevatn ~ *Department of Earth Science, University of Bergen, Allégaten 41, 5007 Bergen, Norway; atle.rotevatn@geo.uib.no*

Atle Rotevatn received his Candidatus Scientiarum degree (M.S. degree equivalent) from the University of Oslo in 2004 and a Ph.D. in structural geology from the University of Bergen in 2007. In 2006, he joined the Norwegian exploration and production company Rocksource, after which (2010) he joined the Department of Earth Science at the University of Bergen, where he is presently professor of structural and reservoir geology.

Eirik Keilegavlen ~ *Department of Mathematics, University of Bergen, Allégaten 41, 5007 Bergen, Norway; eirik.keilegavlen@math.uib.no*

Eirik Keilegavlen holds an M.Sc. (2006) and a Ph.D. (2010) in applied mathematics from the University of Bergen. Since 2012, he has been a researcher in the Department of Mathematics of the University of Bergen. His research focuses on the development of mathematical models and numerical methods for flow and deformation of porous media.

Haakon Fossen ~ *Department of Earth Science, University of Bergen, Allégaten 41, 5007 Bergen, Norway; The Natural History Collections, University Museum of Bergen,*

University of Bergen, P.O. Box 7800, 5020 Bergen, Norway; haakon.fossen@geo.uib.no

Haakon Fossen received his Candidatus Scientiarum degree (M.S. degree equivalent) from the University of Bergen (1986) and his Ph.D. in structural geology from the University of Minnesota (1992). He joined Statoil in 1986 and the University of Bergen in 1996. His scientific interests cover evolution and collapse of mountain ranges, structure and evolution of North Sea rift basins, and petroleum-related deformation structures at various scales.

ACKNOWLEDGMENTS

This study forms part of the Contraction of Porous Sandstones (COPS) project, financed by Statoil and the Centre for Integrated Petroleum Research (Uni Research CIPR). Ingrid Aarnes from Roxar AS provided helpful advice on RMS software. Colleagues at Uni Research CIPR (Jan Tveranger and Dongfang Qu) provided useful feedback and discussions. We are grateful to the reviewers John Solum and Peter Eichhubl and one anonymous reviewer, who all provided useful insights and constructive criticism that greatly improved our manuscript. We are also very grateful to AAPG Elected Editor Mike Sweet and associate editor Rick Groshong, whose editorial guidance and scientific input helped improve the clarity of the final product.

EDITOR'S NOTE

Color versions of Figures 1–3 and 5–7 can be seen in the online version of this paper.

INTRODUCTION

In this study we focus on the factor of deformation bands as structural heterogeneities in hydrocarbon fields within contractional fault-propagation fold traps. Fault-propagation folds are important hydrocarbon traps in fold and thrust belts (e.g., Mitra, 1990), and several of the world's hydrocarbon provinces are found in contractional tectonic settings or settings partially affected by contraction, where such trap types are very common; examples include the Zagros Basin (e.g., McQuarrie, 2004), the South Caspian Basin (e.g., Jackson et al., 2002), and the Aquitaine Basin (e.g., Biteau et al., 2006). Reservoir units within such structures may include porous sandstones, and when folded, these units may accommodate strain by forming deformation bands (Zuluaga et al., 2014). Because deformation bands (Aydin, 1978) have been known to be associated with a reduction in permeability (see Fossen et al., 2007, as well as the following subsection), it is of interest to study their function as flow baffles in such settings. In this study, we use well-exposed deformation band networks within the San Rafael Reef monocline as a structural analog to study reservoir heterogeneities hosted within contractional fault-propagation fold traps. The study site was mapped in detail by Zuluaga et al. (2014) and is a particularly well-suited analog because a link between fold tightness (reflected by the dip of the forelimb) and deformation band occurrence (type and intensity) was established, which may be extrapolated to similar sites elsewhere.

Formation and Detection of Deformation Bands in Porous Sandstone Reservoirs

Deformation bands (Aydin, 1978) are small-scale structural heterogeneities that are common in sandstone reservoirs with porosity greater than or equal to 15%, also known as granulation seams (Pittman, 1981) or shear bands (Menéndez et al., 1996). These millimeter-thick, tabular zones range in length from a few centimeters to over 100 m (~328 ft) and accommodate millimeter- to centimeter-scale shear displacement. They form during deformation of highly porous sandstones, where available pore space facilitates deformation mainly through (1) grain reorganization or (2) cataclasis, caused by stress concentration at grain contact points (for a review, see Fossen et al., 2007). As mentioned above, deformation bands are generally associated with compaction and permeability reductions; previous studies report values ranging from one to six orders of magnitude permeability contrast between deformation bands and host rock but most commonly in the range of two–three orders of magnitude (Crawford, 1998; Sternlof et al., 2006; Torabi et al., 2008). Cementation and dissolution may, however, greatly amplify the permeability reduction, which may explain some of the more extreme values

reported by some authors (Fossen et al., 2007). Given the reported permeability reduction in deformation bands, arrays of deformation bands may compartmentalize reservoirs, alter flow paths, and induce significant permeability anisotropy (Antonellini and Aydin, 1994, 1995; Matthäi et al., 1998; Eichhubl et al., 2004; Sternlof et al., 2004; Fossen and Bale, 2007; Torabi and Fossen, 2009; Ballas et al., 2015). The effect of deformation bands on flow will also depend on the length, orientation, and connectivity of bands because a well-connected deformation band network will more efficiently affect flow, compared with single bands, where fluids will be able to find flow paths avoiding the bands (cf. Rotevatn et al., 2007). In a typical petroleum field setting, the detection of small-scale reservoir heterogeneities is limited by the resolution of seismic data sets. Modern, commercial, high-quality three-dimensional (3-D) seismic data sets can achieve a vertical resolvability of 20–30 m (65–98 ft); however, for older and less sophisticated data sets the resolution may be much lower. Given the small-scale nature of deformation bands, they remain unresolvable by reflection seismic data and wireline logs (Gabrielsen et al., 1998), which leaves their prediction in the subsurface, and their incorporation on geocellular reservoir models, extremely challenging. The prediction of such small-scale structural heterogeneity is possible by relating them to structures that are seismically mappable by means of analog field studies, in combination with a thorough understanding of the reservoir's geology. Where available, core material provides spatially restricted information that may yield clues about the style of small-scale structural heterogeneities to be expected.

Previous Work on the Dynamic Flow Effects of Deformation Bands

Previous studies have addressed the effect of deformation band populations on fluid flow by exploring their distribution and petrophysical properties in damage and process zones of faults. Most previous studies are limited to extensional tectonic settings, where the deformation bands tend to be localized in the vicinity of faults (Antonellini and Aydin, 1995; Rotevatn et al., 2009, 2013; Rotevatn and Fossen, 2011; Schueller et al., 2013). In comparison, there are few studies on the permeability effects of deformation bands in contractional tectonic settings, despite evidence that in this setting, the deformation bands are reported to be more widely distributed than those formed in the extensional regime (Solum et al., 2010; Brandenburg et al., 2012; Soliva et al., 2013; Fossen et al., 2015). This difference in spatial distribution might have an effect on overall sweep and flow trajectories. Fluid flow across contractional deformation band populations has been explored to some extent (e.g., Lewis and Couples, 1993; Sternlof et al., 2006; Rotevatn et al., 2013; Deng et al., 2015); however, to date, the effect of deformation bands on fluid flow in contractional fault-propagation folds has not been explored.

Study Goals

We investigate the effect on fluid flow of deformation band arrays formed in the forelimb of a contractional fault-propagation fold along the east margin of the San Rafael Swell, i.e., the San Rafael monocline in southeast Utah (Figure 1). Combining structural field data from Zuluaga et al. (2014) with multiscale approaches to fluid flow simulation, we incorporate and evaluate the effects of deformation bands on fluid flow across the structure. The main goal of this is to use the site as a structural analog to quantify the effect of the deformation bands on flow; to make the study applicable to a wide range of settings globally, we omit effects of local stratigraphy (stratigraphy is modeled as a homogeneous sand) because introducing additional heterogeneities would serve to cloud the results and mask the effects of the deformation bands. This is done because the purpose of the exercise is to test the effect of structural heterogeneity on flow; site-specific production performance or production optimization is beyond the scope of this study.

The basis for the geocellular model and flow simulations of this study are based on structural outcrop data presented in Zuluaga et al. (2014) supplemented with geological and digital elevation data sets. The flow simulations presented herein cover a five-order-of-magnitude range of deformation band permeabilities that includes those measured in the field, as well as those recorded by other studies (Taylor and Pollard, 2000; Sternlof et al., 2004); we aim to constrain the effects of subseismic deformation on effective reservoir permeability and to simulate production performance and flow dynamics. Specifically, this study aims to do the following.

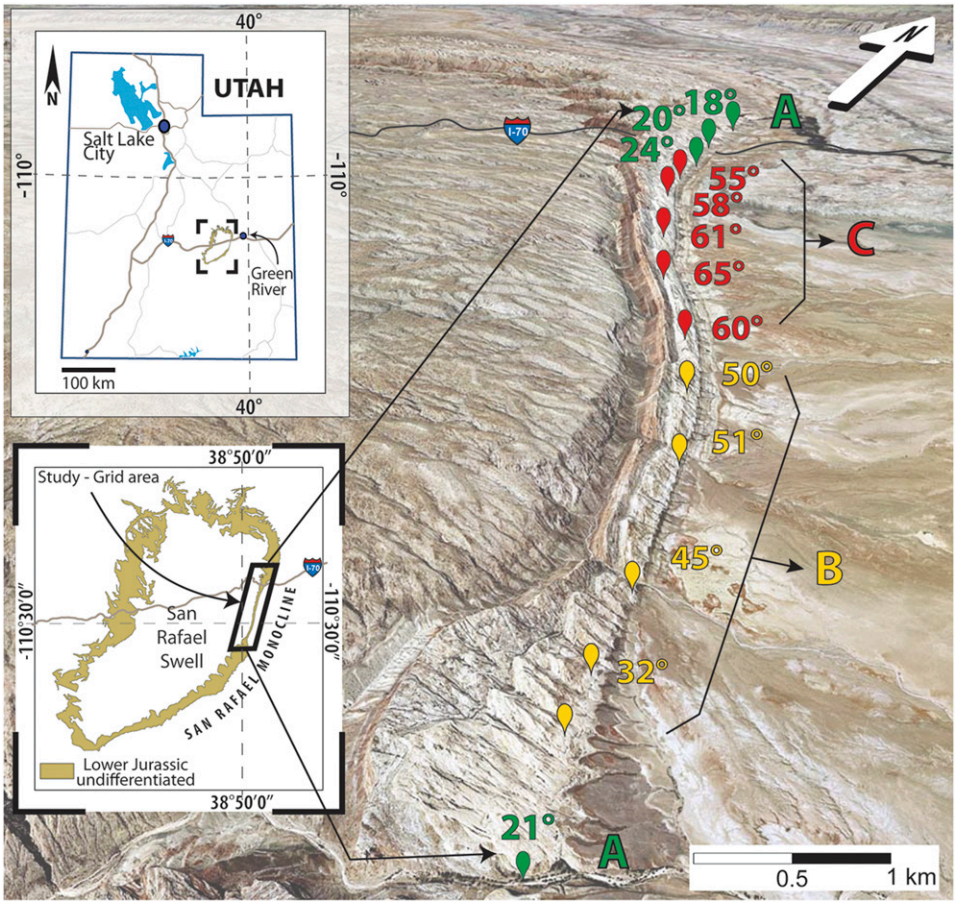

Figure 1. Aerial photograph of the outcropping rocks in the study area with visited localities and corresponding forelimb dip domains: gentle (indicated by A), intermediate (indicated by B), and steep (indicated by C). Detail of location (top inset) and surface expression of the Navajo Sandstone in the San Rafael Swell and its forelimb, the San Rafael monocline (bottom inset). Study area for grid construction is delineated by the polygon, corresponding to the steepening part of the monocline.

1. Evaluate the effect of subseismic reservoir heterogeneities on fluid flow in contractional folds by means of outcrop-based flow simulations.
2. By doing so, develop geologically meaningful upscaling strategies for the incorporation of structural heterogeneities below the resolution of geocellular simulation grids.
3. Discuss the overall effects on reservoir properties and performance and the applicability in comparable structural settings.
4. Offer insight that relates seismically mappable structures (i.e., prospects or fields) to subseismic structural heterogeneities and their effect on flow.

GEOLOGICAL SETTING

The outcrop studied herein belongs stratigraphically to the eolian Navajo Sandstone in the eastern flank of the San Rafael Swell, i.e., the San Rafael monocline (Figure 1). This Jurassic unit is composed of cross-bedded, white to tan weathering, well-rounded, well-sorted, fine- to medium-grained quartz-rich sandstone deposited in an eolian environment during the Early to Middle Jurassic (Fischer and Christensen, 2004) with a present-day porosity of approximately 20% and darcy-scale permeability. The Swell is a north–northeast-striking, doubly plunging, asymmetric fault-propagation fold (Doelling, 2002) approximately 120 km (~75 mi) long and 60 km (37 mi) wide in the northwestern Colorado Plateau, located approximately 25 km (15 mi) west of Green River in Emery County, Utah (Figure 1).

The Swell belongs to a series of basement uplifts in the Colorado Plateau that are generally (but not universally) interpreted to have evolved in the Late Cretaceous to Eocene, as Laramide contraction took advantage of preexisting weaknesses in the Precambrian basement rocks (Dickinson and Snyder, 1978; Hintze, 1988; DeCelles and Coogan, 2006), forming steep contractional faults with fault-propagation folds above. The underlying fault offsets Precambrian to Paleozoic rocks, folding the overlying Mesozoic sequence (Tindall and Davis, 1999; Marshak et al.,

2000). Other examples of such uplift structures include the East Kaibab monocline in in northern Arizona and southern Utah, the Waterpocket Fold south of San Rafael Swell, and the Colorado National Monument in western Colorado (Davis, 1999; Jamison and Stearns, 1982). Whereas most of the Swell is associated with a very gently dipping backlimb, the narrow eastern flank is characterized by a monocline with forelimb dips reaching 65° (Doelling, 2002). This steep, eastern, monoclinal segment of the swell is known as the San Rafael monocline and forms the basis for this study (Figure 1). Here the Jurassic Navajo Sandstone, approximately 120–200 m (390–650 ft) thick in the study area, is exposed continuously along strike, in cliff sections that are accessible through several slot canyons that cut into the monocline. The Navajo Sandstone in the monocline is affected by arrays of cataclastic deformation bands (Bump and Davis, 2003; Zuluaga et al., 2014), creating a flow retarding effect that represents the focus of the present study, In general, the Navajo Sandstone is widely recognized as a reservoir unit (Beitler et al., 2003; Parry et al., 2009), and in the study area, paleo–fluid flow can be inferred

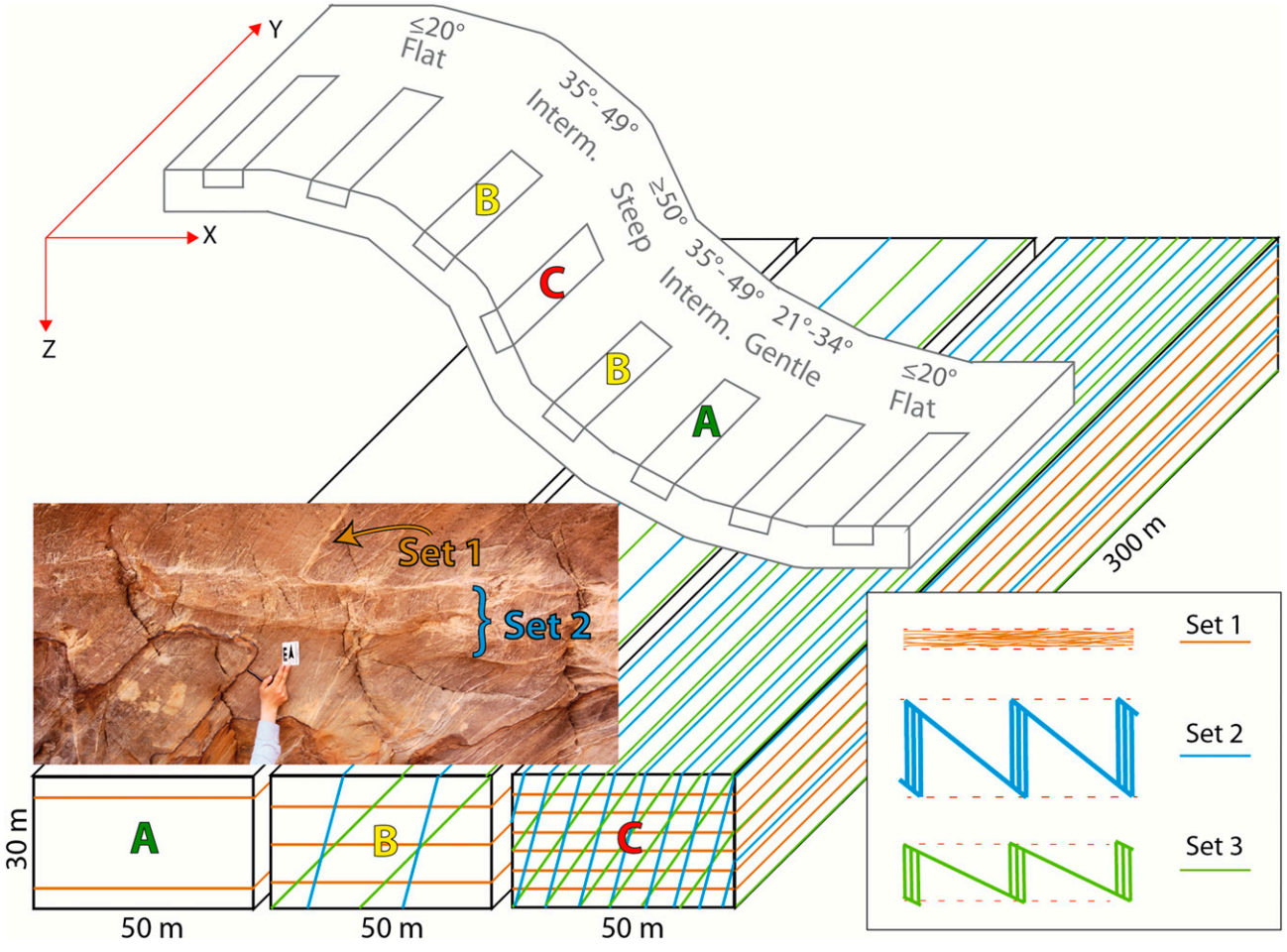

Figure 2. Top: simplified sketch of the monocline reconstruction, with resulting grid cells according to dip domain. Middle left: Photograph showing deformation band arrays in the field (set 3 not shown). Notice red–brown paleo–fluid front (bottom left of the photograph) influenced by the band geometry and a ladder structure (set 2) offsetting a deformation band array of bedding parallel deformation bands (set 1). Bottom right: detail of deformation band sets: set 1 (strands–clusters) and sets 2 and 3 (conjugated ladder structures of variable thickness). Maximum thickness for each set is 2.5 cm (1 in.) for set 1, 50 cm (2 ft) for set 2, and 30 cm (1 ft) for set 3. Bottom left: resulting cell dimensions and deformation band geometries with corresponding arrangements and frequencies according to dip domains or bins (cases A, B, and C). Deformation bands of set A follow bedding (in orange) deformation bands of sets 2 and 3 cross-cut bedding (blue and green). Notice that cells in flat domains do not contain any deformation bands; thus, intact host rock properties are maintained for cells in flat domain areas. Interm. = intermediate. Note: A color version can be seen in the online version.

Table 1. Spatial Characteristics of Deformation Band Arrays in the San Rafael Monocline

Category	Thickness	Spacing	Length		Continuity		Connectivity	Dip Bins (Domains)		
			Along Strike	Across Layering	Along Strike	Across Layering		Gentle Case A	Intermediate Case B	Steep Case C
Set 1	0.1 to 10 cm (0.04 to 3.94 in.)	Not uniform	≤10 m (32.8 ft)	U	Good	Poor	Good	X	X	X
Set 2	10 to 150 cm (3.94 to 58.8 in.)	3–5 m (9.84–16.4 ft)	5–10 m (16.4–32.8 ft)	10–50 m (32.8–164 ft)	Moderate	Good	Moderate		X	X
Set 3	1–5 cm (3.28–16.4 ft)	1.5–2.5 m (4.9–8.2 ft)	U	15–20 m (49.2–65.6 ft)	U	Poor	None			X

Abbreviation: U = uncertain.

from the abundant bleaching patches throughout the sandstone unit, some of which are fluid fronts interrupted by deformation band arrays (see photograph in Figure 2).

DEFORMATION BANDS IN THE SAN RAFAEL MONOCLINE

Readers are referred to Zuluaga et al. (2014) for a detailed structural account of the study area; in the following, a short description of the deformation band arrays relevant for the flow simulation is provided, as context for the present study (Tables 1, 2). Field data were collected along strike of the monocline in several canyons having cut into the structure's forelimb. The structural data collected included spacing, frequency, thickness, and character of deformation bands, as well as probe permeameter measurements (Tables 1, 2). In Zuluaga et al. (2014) it is shown that deformation band populations are restricted to the steeply dipping part of the forelimb of the fold (Figure 1), beginning to appear in the Navajo Sandstone where the forelimb dip of the monocline reaches approximately 30°. In these dip domains, deformation bands follow sedimentary crossbeds (set 1 in Figure 2). As the folding increases into intermediate and steep dip domains, deformation bands of set 1 progressively increase in number and thickness, and new deformation bands arranged in conjugate sets of ladder structures appear (sets 2 and 3 in Figure 2); these ladder structures cross cut bedding and, consequently, offset deformation bands of set 1 as well (Figure 2, photograph). All three sets of deformation bands get increasingly thicker up to the maximum forelimb dip of approximately 65°. The present paper builds on this study, aiming to assess the effect of the previously described structures on fluid flow. Here we use the structural data to construct a geocellular reservoir model, the methodology of which is described in the grid modeling section of this paper.

Because all sets display higher development and frequencies of deformation bands as the folds steepens, a relationship between dip of the Navajo surface was correlated to the strain in the sandstone interval and, hence, to the amount, type, and arrangement of deformation bands present. Using this relationship, the entire surface of the Navajo Sandstone was subdivided into four dip domains (dip bins). According to the

Table 2. Input Parameters of Deformation Bands in the San Rafael Monocline

	DB Set 1			DB Set 2			DB Set 3		
Dip Bins	DB/m	Max Bandwidth (m [ft])	Angle (°)	DB/m	Max Bandwidth (m [ft])	Angle (°)	DB/m	Max Bandwidth (m [ft])	Angle (°)
A′ (21°–34°)	0.2	0.0025 (0.008)	0					Not developed	
B′ (35°–49°)	1.4	0.0025 (0.008)	0	0.47	0.0075 (0.0246)	45	0.27	0.0075 (0.0246)	75
C′ (≥50°)	5	0.025 (0.08)	0	1.1	0.015 (0.049)	55	0.45	0.015 (0.049)	85

Input parameters are thickness, frequency, spacing, and angular relationships. Angles are relative to the base of the cell; refer to Figure 2 for set geometry.
Abbreviation: DB = deformation bands; Max = maximum.

steepness of its top surface, each bin was set to contain increasing amounts and more complex arrangements of deformation band sets in the sandstone interval: (1) areas where the surface dips 0° to 20° are barren of deformation bands and are considered to be flat; (2) areas where the surface dips lie between 21° and 34° contain widely spaced deformation bands of set 1 only and are hereafter referred to as gentle (case A in Figure 2); (3) areas with surface dips of 35° to 49° are considered intermediate dip domains, containing more, thicker and closely spaced deformation bands from set 1, in addition to thin arrays of sets 2 and 3, which are widely spaced (case B in Figure 2); and finally, (4) steep dip domains are areas in which surface dips are equal to or higher than 50°, containing more closely spaced and thicker arrays of deformation bands than all three sets (case C in Figure 2).

Structural mapping across several canyons of the monocline and in situ permeability measurements (Zuluaga et al., 2014) allowed us to estimate the spatial distribution and petrophysical properties of deformation bands and their intact host rock, and these data were fed into the numerical model. By using a surface analog with widespread exposure it is possible to constrain 3-D spatial distributions of deformation bands in zones with variable strain to improve permeability estimations for reservoir models, commonly assumed by typically limited and scattered data (constant values, averages of core plug measurements, etc.).

GRID MODELING AND FLUID FLOW SIMULATION DESIGN

Emerson Process Management's reservoir modeling suite Roxar RMS 2012 was used in this study. This is an industry standard software package that allows a complete modeling workflow, from basic grid construction to flow simulation of property-filled grids. The explicit inclusion of the deformation bands in the simulation model would, however, be prohibitively computationally expensive, and the bands are therefore accounted for by a local upscaling of permeabilities on an unstructured grid, which is adapted to the deformation band geometry. Details on the upscaling are given further below.

Model Framework and Grid

The framework for the geological reservoir model comprises the top and base of the Navajo Sandstone. The top Navajo Sandstone horizon surface in RMS was created by interpolation of digitized structural contours of the unit from the geological map of the area (Doelling, 2002); in structurally (and topographically) higher parts of the monocline where erosion has removed the Navajo Sandstone (Figure 3A), structure contours from the underlying Chinle top Formation were used as guide to reconstruct the top Navajo surface geometry. Assuming a total Navajo thickness of 200 m (656 ft), the base Navajo was approximated as an identical surface 200 m (656 ft) below the top Navajo (Figure 3B). The geocellular grid was created between these two surfaces, restricted to the steepest segment of the monocline (i.e., the area affected by deformation bands) and surrounding gently dipping segments. The grid was divided in three bedding-parallel zones of equal thickness to account for sedimentary layers.

The resulting modeling grid has a total grid size of 16 km × 25 km × 200 m (10 mi × 15 mi × 656 ft) and a structural relief of 1.6 km (1 mi) (Figure 3, Table 3). The grid comprises 356 × 86 × 3 cells, bringing the total number of grid cells to 91,848. The

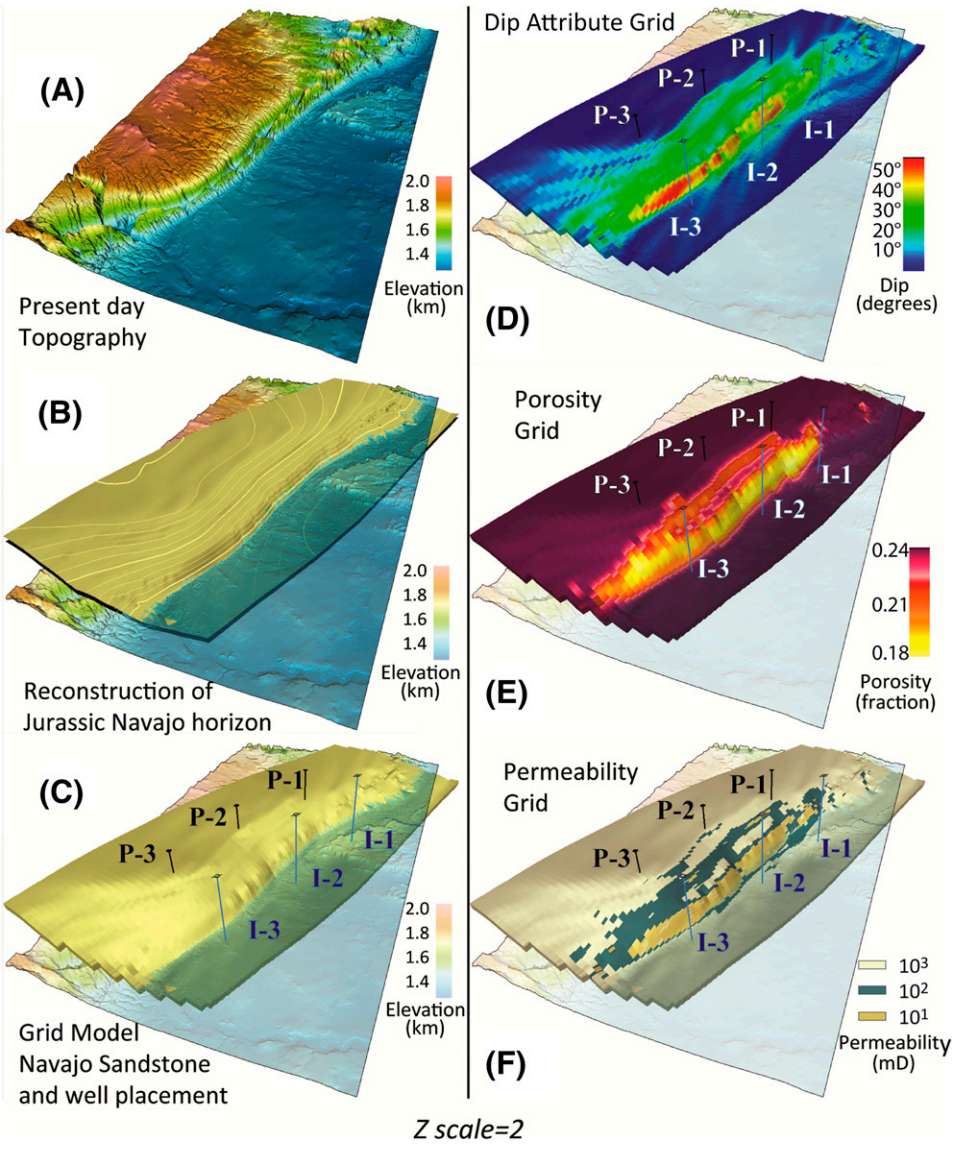

Figure 3. Stages of grid construction and property modeling. (A) Reconstruction of reservoir grid from present-day topography, (B) Navajo Sandstone horizon creation from geological data, and (C) grid construction and well placement. Injectors are placed downdip in the lower limb, and producers are at the upper limb, in the crest of the monocline. Grid parameter population from field observations: the surface of the grid allowed the generation of (D) a dip attribute parameter, used henceforth to constrain and populate the grid cells with (E) porosity as well as (F) permeability values.

average cell size of the grid is 50 × 300 × 30 m (164 × 984 × 98.4 ft) as seen in Figure 2; the reason for the disproportionately large grid cell dimension in the Y dimension is that the structures recorded in the field are relatively parallel to the monocline limb itself, and the long axis of the grid cells should ideally be parallel to the main geological heterogeneity. The overall large grid cell size of this model, and reservoir models in general, makes upscaling necessary to incorporate the effect of deformation bands in the model.

Modeling of Petrophysical Properties

Because the main objective of the flow simulations is to capture and isolate the effect of deformation bands from folding strain on flow in high-quality reservoirs, lithological contrasts were omitted, and the reservoir sedimentology was modeled as homogeneous because high-quality reservoirs such as eolian sandstones are considered relatively homogeneous, and lithological variations are a relatively minor factor in permeability anisotropy (Corbett and Jensen, 1993). Petrophysical properties of intact host rock were based on field measurements (Zuluaga et al., 2014), with 25% porosity and 1000 md permeability maximums. Where applicable, porosity and permeability were then modified to account for the presence of deformation bands, following the procedure described below.

The permeabilities used in the simulation model should account both for the permeability contrast

Table 3. Grid Properties

Property	Value
Total grid size	16 × 25 km (10 × 15.5 mi)
Structural relief	~2 km (1 mi)
Number of cells	91,848
Average cell size (x, y, z)	50 × 300 × 30 m (164 × 984 × 98 ft)

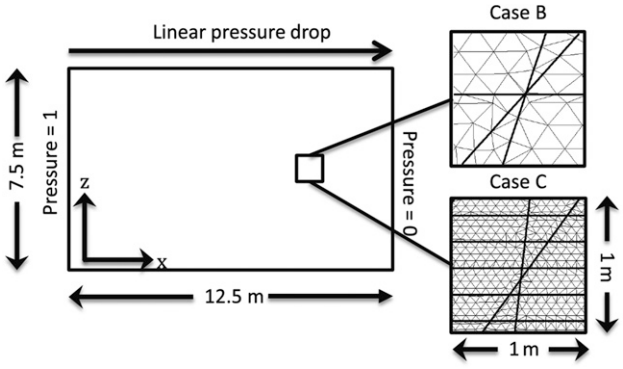

Figure 4. Illustration of the auxiliary domains, and the setup for upscaling of K_x. The entire domain is populated with bands from either case B or C.

between bands and host rock and for band geometry. For case A in Figure 2, the band geometry is aligned with the coarse cells, and the bulk permeability can be computed analytically by the arithmetic mean parallel to the bands (the x direction in Figure 4) and by the harmonic mean in the cross-band direction. For cases B and C in Figure 2, the bands run with an angle to the natural directions in the individual grid cells, and therefore, they do not lend themselves naturally to computations on structured (Cartesian-like) grids. A field-scale simulation model based on an unstructured grid that explicitly represents the bands would, however, have a prohibitively high cost; as a compromise for cases B and C, upscaled permeabilities are computed in a local approach using small, auxiliary, computational domains (see Figure 4). The permeability in the direction parallel to the monocline strike, K_y, can be computed from an arithmetic mean with the host rock permeability, and the auxiliary domains were therefore taken as two-dimensional, representing the direction perpendicular to the strike of the monocline and the vertical direction, rendering permeabilities K_x and K_z, respectively.

Based on initial sensitivity studies, auxiliary domains of size 12.5 × 7.5 m (41 × 25 ft) were found to cover a sufficient number of each set of deformation bands to give a meaningful computation of upscaled permeabilities, which can be employed in the large-scale simulations (compare with Table 2; see also Rotevatn et al., 2013, for an example of a similar sensitivity study). In the auxiliary domains, triangular grids were constructed to be conforming to the deformation bands (Figure 4), thus resolving the permeability heterogeneity. Because the deformation bands are narrow compared with the domain size, the explicit gridding inside the deformation bands would either require a prohibitively high number of cells or yield grids with very sharp angles, which may pose problems for the calculations. An alternative approach, originally developed for flow simulations in fractured media (Karimi-Fard et al., 2003), is to treat the deformation bands as a lower-dimensional object (in this case a line) in the gridding process and only include the bands in the discretization. The approach is based on the standard two-point flux commonly employed in commercial reservoir simulations and has been validated and employed also in low-permeability structures such as compaction and deformation bands (Sternlof et al., 2006; Sandve et al., 2012; Rotevatn et al., 2013). Based on this approach, upscaled permeabilities were computed by solving the pressure equation on the local domain with the following boundary conditions: The flow was forced by assigning unit pressure on one side and zero pressure on the opposite side, say, in the x direction (ΔX), and then assigning a linear pressure drop (Δp) between the two other sides (see Figure 4 for an illustration, and also Durlofsky, 2003). The bulk permeability was then computed from

$$K_x = \frac{q_x \Delta X}{\Delta p}$$

with q_x computed as the averaged flux in the x direction. A similar calculation with pressure drop in the z direction rendered K_z. The procedure was carried out for both cases B and C.

To test the sensitivity of production performance and flow dynamics to different degrees of deformation band permeability, a range of scenarios were considered with a contrast to the intact host rock spanning from zero to five orders of magnitude

Table 4. Overview of *X*, *Y*, and *Z* Permeabilities Assigned to Cells for Each Flow Scenario and Dip

Scenarios	Permeability Direction	Permeability of Dip Bins (md)			
		Host: ≤20°	Case A′: 21–34°	Case B′: 35–49°	Case C′: ≥50°
S5: 10^5 (hr = 1000 md; DB = 0.01 md)	K_X	1000	1000	2.5	0.43
	K_Y	1000	1000	991	852
	K_Z	1000	19.6	2.6	0.08
S4: 10^4 (hr = 1000 md; DB = 0.1 md)	K_X	1000	1000	23.9	4.3
	K_Y	1000	1000	991	852
	K_Z	1000	167	24.9	0.8
S3: 10^3 (hr = 1000 md; DB = 1 md)	K_X	1000	1000	184	41
	K_Y	1000	1000	991	852
	K_Z	1000	667	189	7.9
S2: 10^2 (hr = 1000 md; DB = 10 md)	K_X	1000	1000	624	293
	K_Y	1000	1000	991	853
	K_Z	1000	953	607	72
S1: 10^1 (hr = 1000 md; DB = 100 md)	K_X	1000	1000	889	765
	K_Y	1000	1000	992	867
	K_Z	1000	996	833	391
S0: No contrast (hr = 1000 md; DB = 1000 md)	K_X	1000	1000	1000	1000
	K_Y	1000	1000	1000	1000
	K_Z	1000	1000	1000	1000

Abbreviations: DB = deformation bands; hr = host rock.

permeability reduction of deformation bands (zero being a control scenario of the unit without deformation bands). The reason for the wide range of permeabilities chosen was to cover (1) the range of permeabilities reported in the field study (Zuluaga et al., 2014), (2) permeability reductions most commonly reported in the literature of one–three orders of magnitude (e.g., Fossen et al., 2007), and (3) the more severe values reported (some report band permeabilities as low as 0.001 md; e.g., Freeman, 1990; Antonellini and Aydin, 1994; Knipe et al., 1997; Fisher and Knipe, 2001; Shipton et al., 2002) related to very well–developed cataclasis or secondary cementation of the bands. The resulting upscaled permeabilites computed for cases A–C and all contrasts are presented in Table 4.

The permeability values computed for the auxiliary domains were then mapped to the simulation model. Because layer steepness is an indirect measure of strain, and thus a controlling factor in the amount of deformation bands encountered, an attribute map describing the dip of the top surface was created, which in turn was used to generate a parameter that assigned an average dip value to each cell (Figure 3D). Using the deformation band dip bins described previously, the dip parameter was in turn used to classify the grid cells into each of the three dip bins, providing a link between dip, deformation band occurrence, and resulting permeability for the 3-D simulation grid. The permeability values computed as described before were then used to populate the grid. Porosity modeling was also controlled by the dip attribute map; flat domains remained with the maximum porosity of 25%, whereas for increasingly dipping cells, values were set to range down to a minimum of 18%. In this way, the 3-D simulation grid was populated with modified petrophysical properties to account for the presence of deformation bands and prepared for 3-D flow simulations. As for the single cross beds within layers, the relative effect of their heterogeneity compared with that of the deformation bands is negligible; in addition, this study deals with relative permeability, and because deformation bands permeability vary significantly, this is analogous to varying the matrix permeability.

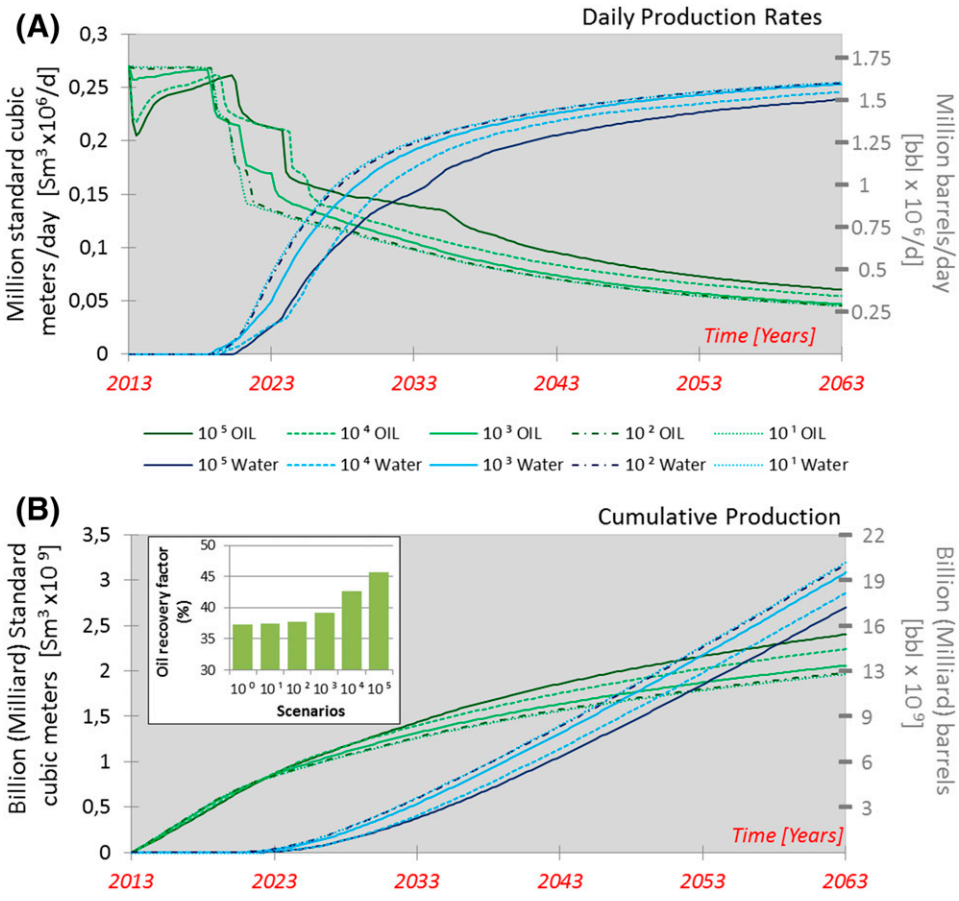

Figure 5. Flow simulation results for all permeability contrast scenarios. (A) Daily production rates in million standard cubic meters per day (left axis) and in million barrels per day (right axis). Notice the steps in the green (online version) curves representing water cuts at each of the three producing wells. (B) Total cumulative production volumes in milliard standard cubic meters (left axis) and in billion barrels (right axis). Subset bar graph in Figure 5B represents recovery factor for each scenario.

Experimental Design

For the field-scale flow simulations, a total of five models corresponding to the previously mentioned 10^1 to 10^5 orders of magnitude permeability contrast between host rock and deformation bands plus a control scenario (with no deformation bands) were built, and flow was simulated using the RMS finite difference, black oil simulator (Figures 5, 6). The dynamic properties used to condition the models are summarized in Table 6 in the Appendix. Because the main aim was to investigate the effects of the deformation bands on flow through the monocline, typical midrange properties were used and kept constant for all model runs. The flow simulations were based upon three vertical water injection wells and three vertical production wells. The injection wells were placed with a spacing of 5 km (3 mi) at the base of the model slope; the production wells were placed with a similar spacing at the crest of the monoclinal grid (Figure 3C). The shortest distance from each injection well to the nearest production well is 3 km (2 mi). The aim was to simulate injection in the lower part of the model and evaluate flow across the grid for 50 yr. Because of the large size of the model, the following simplifications were necessary: first, completion and perforation intervals of the wells covered the entire 200-m (656-ft) thickness of the drilled grid (for comparison, only 40 m (131 ft) out of the 137 m (449 ft) hydrocarbon column is open and completed in Covenant wells, a nearby field producing from the same unit); second, extreme injection rates of 100,000 Sm^3 of water per day (~628,000 BWPD) and production rates of 90,000 Sm^3 oil production per day (~566,000 BOPD) were used; and third, the reservoir was assumed to be oil-filled, (i.e., oil–water contact below the geocellular model).

RESULTS

The flow simulation results of all scenarios are shown in Figure 5. As anticipated, increasing contrasts in permeability resulted in lower production rates and delayed water breakthroughs; however,

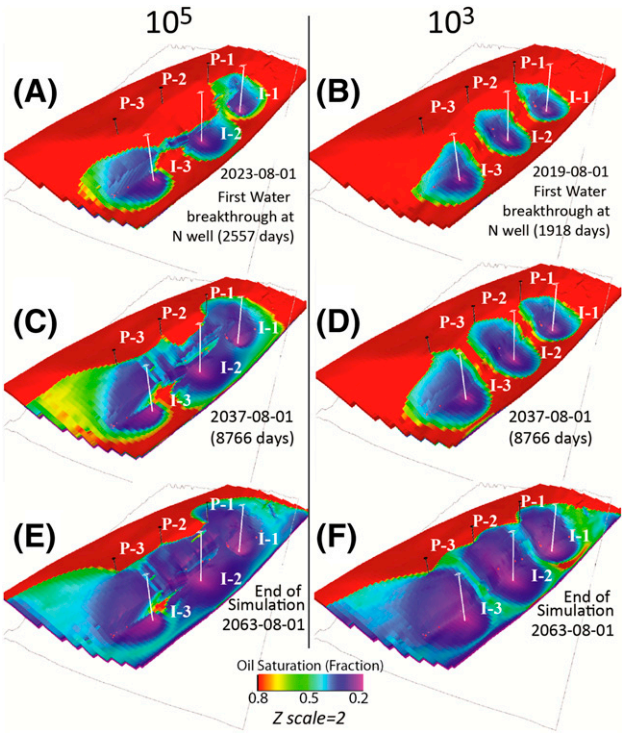

Figure 6. Flow simulation results viewed from the top Navajo grid for scenarios 10^5 (A, C, E) and 10^3 (B, D, F). (A) and (B) show grids at first water breakthroughs, both at Producer-1 (northernmost) well; (C) and (D) show differences in flow pattern for both scenarios at the same time into simulations. Notice the higher flow anisotropy and flow redirection in *y* axis for 10^5 (C). (E) and (F) show grids at the end of simulations for both scenarios. See text for full discussion. I = injector wells; P = producer wells.

production trends and individual well behavior varied among scenarios. Generally, scenarios including up to 10^2 host to deformation band permeability contrast behaved quite similarly, whereas from 10^3 permeability contrast onward, the production performance was increasingly affected by the structural heterogeneity represented by the deformation bands.

Total volumes of oil produced range from 1.9 to 2.4 billion Sm^3 (~12.4 to 15 billion bbl) from 10^1 and 10^5 permeability contrast scenarios, respectively, with recovery factors ranging from 37.4% (10^1) to 45.7% (10^5) (Figure 5B). As mentioned, volumes produced are very similar up to 10^2 permeability contrasts, with the control scenario of 10° being virtually undistinguishable from the 10^1 scenario, whereas the results are highly variable for the remaining three higher-contrast simulations.

Scenarios 10^1 and 10^2 show constant daily production rates of 270,000 Sm^3 (~1.7 million bbl) per day for the first 5 yr, which subsequently decline rapidly following initial water breakthrough. In contrast, scenarios 10^3, 10^4, and 10^5 display (1) an initial decline in daily production rates (less marked in 10^3 scenario) that (2) subsequently increase steadily to 270,000 Sm^3/day (~1.7 million bbl/day), after which (3) steady decline onsets following water breakthrough. Scenario 10^5 has the most gradual decline in oil daily production, with water breakthroughs occurring in long time intervals: the first well water cut occurs 7 yr into the simulation, the second arrives 3 yr after the first, and the last well starts producing water 12 yr after the previous well, i.e., 22 yr since the start of the simulation, thus providing most of the field's oil production over time for this case. Scenario 10^1 records the fastest decline in daily production rates, with short time intervals between well water cuts, the first happening 5 yr into the simulation, followed by 2 more years before the remaining two wells undergo water breakthrough within months of each other (see breaks in green curves of Figure 5A).

At the end of the simulation, scenarios 10^1 to 10^3 converge to very similar oil and water daily productions, whereas 10^4 and 10^5 maintain comparatively higher oil daily productions, with notably different water-to-oil ratios between wells (see Figure 7). The delay in water breakthrough is also reflected in total produced volumes at the end of simulation runs: the models with progressively less-permeable deformation bands experience progressively delayed water breakthrough and, thus, a prolonged production life. This leads to better results in terms of produced volumes and total recovery. This effect is seen from the 10^3 scenario onward but is particularly evident for scenarios 10^4 and 10^5 (Figure 5B, inset).

DISCUSSION

The Effect of Deformation Bands on Flow in the Models

The results of the flow simulations presented herein show that although complete blocking of flow is not occurring, they are clearly causing partial redirection of fluid flow in the reservoir. Ten years into the simulation in the higher-contrast scenarios (10^4 and 10^5), it is evident that fluids are partially channeled in the direction of less permeability

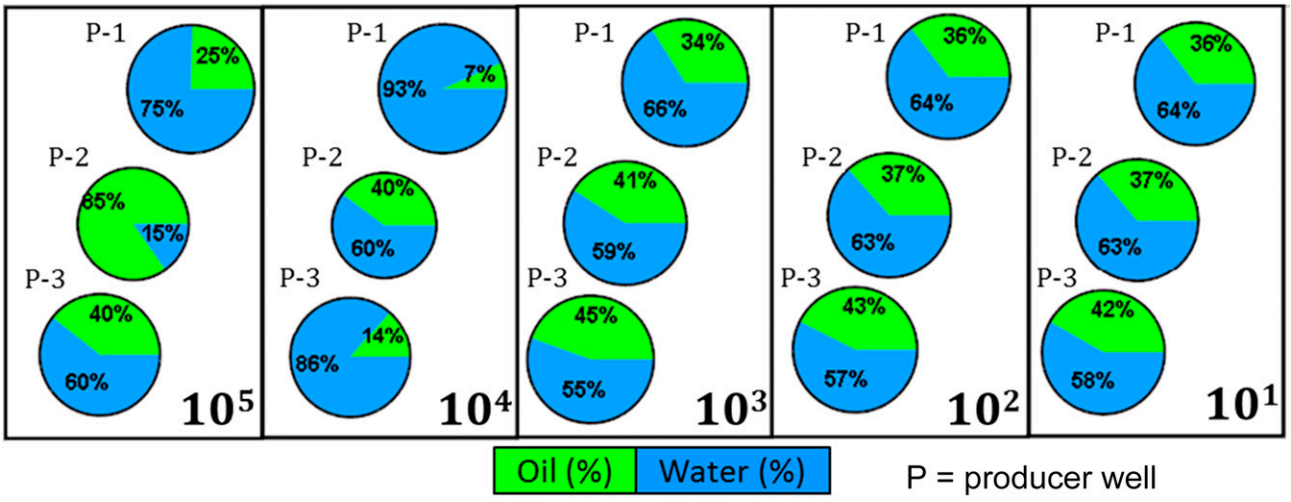

Figure 7. Pie charts showing percentage of fluid production per well at the end of the five flow scenarios of flow simulation (pie chart radii are proportional to the total volumes produced). Notice similarity between low-permeability contrast scenarios (10^3, 10^2, and 10^1), whereas 10^5 and 10^4 scenarios differ notably with the lower-contrast cases, as well as with each other. High-contrast scenarios not only produce notably different percentages of oil and water per well but also differ in the total volumes produced (dissimilar pie charts radii), whereas low-contrast scenarios produce similar total volumes (similar pie chart radii) and similar share of oil and water percentages for all three wells.

anisotropy (*y* direction, subparallel to the deformation bands), especially in the highest-contrast scenarios (see Figure 6A, C, E). This increased flow tortuosity in the higher-contrast scenarios is the cause of their delayed water breakthrough when compared with the other scenarios but also of the order in which the well water cuts occur (Figure 7): for the 10^3 case and lower, the water breakthrough sequence is north to south (P-1 before P-2 and finally P-3), whereas in cases 10^4 and 10^5 the middle well (P-2) is the last to produce water. Flow in the *y* direction is favored in the 10^5 scenario, whereas it is more uniform in the 10^3 one. This flow anisotropy is also evident when comparing percentage of oil versus water produced at simulation final stages: very similar for low-contrast scenarios and highly variable for 10^4 and 10^5 cases. From this it is clear that when deformation bands are absent or relatively highly permeable, dip-parallel flow between injector–producer pairs dominates. For the two cases with the lowest-permeability deformation bands (10^4 and 10^5), however, lateral strike-parallel flow redirection occurs as the injection fluids are forced to flow around the zone of low-permeability bands in the steep limb of the monocline.

In every scenario, however, the northernmost production well (P-1) is always the first to produce water (Figure 6); this is because in addition to having the closest vertical proximity with an injector well (I-1), the injector–producer pair is located in a grid sector in which the grid geometry is not very steep, and thus, the dip attribute also affects the number of deformation bands modeled and the resulting permeability behavior in this area (see Figure 3F).

In terms of recovery and total produced volumes, the 10^3, 10^4, and 10^5 cases show higher production volumes compared to the 10^1 and 10^2 cases (Figure 5, Table 5). Thus, lowering deformation band permeability appears to improve production performance and recovery rates in the models. This occurs because of the increased flow tortuosity caused by the deformation bands, which leads to increased sweep efficiency in the models with lower-permeability bands. Although it may appear as surprising that low-permeability baffles may improve production performance, the results are further supported by similar finds for discontinuous shale bodies (Jackson and Muggeridge, 2000) and deformation bands in relay ramps (Rotevatn et al., 2009).

An outstanding question that remains is how significant deformation bands would realistically be in real subsurface reservoirs. First, deformation bands will generally not have a catastrophic effect on reservoir fluid flow and are unlikely to effectively compartmentalize reservoirs. However, despite the fact that deformation bands may not completely

Table 5. Summary of Production Results

Scenarios	Total Produced Volumes Oil		Total Produced Volumes Water		Total Recovery Factor (%)	Water Breakthroughs					
						First		Second		Last	
	$Sm^3 \times 10^9$	bbl $\times 10^9$	$Sm^3 \times 10^9$	bbl $\times 10^9$		Days into Simulation	Well	Days into Simulation	Well	Days into Simulation	Well
10^5 (hr = 1000 md; DB = 0.01 md)	2.4	15	2.7	17	45.7	2557	P-1	3836	P-3	8035	P-2
10^4 (hr = 1000 md; DB = 0.1 md)	2.2	14	2.9	18	42.7	2191	P-1	4018	P-3	4475	P-2
10^3 (hr = 1000 md; DB = 1 md)	2.1	13	3.1	19	39.2	1918	P-1	2741	P-2	3560	P-3
10^2 (hr = 1000 md; DB = 10 md)	1.98	12.5	3.2	20	37.7	2010	P-1	2465	P-2	2922	P-3
10^1 (hr = 1000 md; DB = 100 md)	1.96	12.4	3.2	20	37.4	2019	P-1	2020	P-2	2021	P-3

Total produced volumes in milliard standard cubic meters and billion barrels. Case 10^0 not shown. Notice water breakthroughs are immediate in case 10^1.
Abbreviations: DB = deformation bands; hr = host rock; P = producer well.

hinder fluid flow, they represent flow baffles and may redirect or perturb flow, leading to increased flow tortuosity and therefore also potentially enhance sweep efficiency. Direct evidence for bands affecting fluids is found in studies that document fluid alteration (oxidation, reduction, and precipitation) that is restricted by deformation bands (e.g., Eichhubl et al., 2004; Ballas et al., 2012). Therefore, deformation bands, although not efficient seals, may affect reservoir flow dynamics and should therefore be taken into consideration in reservoir characterization and production management. Given that deformation bands are generally undetectable from seismic data, their detection in the subsurface, as well as characterization of their petrophysical properties, is reliant on wellbore data. When deformation bands are detected, surface analog studies such as the present study may help understand their distribution and potential effects on flow.

Representation of Deformation Bands in the Reservoir Models

Discrete representation of subcentimeter-scale deformation bands in reservoir models is prohibitively computationally expensive, and an implicit approach is therefore necessary to incorporate their effect in flow simulations. The staged approach used in this study has several advantages. First, computation of upscaled permeability in smaller domains allows for more realistic upscaled permeabilities than that of analytical approaches used in other studies (cf. Rotevatn et al., 2009). Second, the relationship between deformation band intensity and limb dip is exploited when populating the large grid with upscaled permeabilities, thereby establishing a link between model geometry and geological permeability heterogeneity. Similar upscaling techniques that make use of combinations of small and large simulation domains, and which exploit simple geometric relationships, may help industrial geoscientists to build better and more realistic reservoir simulation models.

Applicability, Implications, and Limitations

Folds in general, and contractional fault-propagation folds specifically, are typical hydrocarbon trap forming structures. Thus, understanding how geological heterogeneity and flow dynamics interact in such settings is important for the prediction of flow and optimization of production strategies. Because of the wide range of deformation band permeabilities used in this study, as well as the link used between dip attribute and deformation band geometry and abundance, the results of this study have potentially wide applications in comparable traps and reservoirs.

Although one should be cautious to directly apply the relationships between bedding dip and deformation band occurrence of this study, which are specific to the case studied herein, a similar approach may be applied to subsurface oil fields if similar case-specific relationships may be established based on analog studies or core data. Such application of the current study must consider the local geologic setting, such as sand composition and mineralogy, grain size, porosity, and burial depth at the time of deformation. Although local conditions may not favor the formation of cataclastic deformation bands, other flow-baffling structures may be present, such as framework phyllosilicate deformation bands (Fisher and Knipe, 2001) or minor faults. In carbonate reservoirs and tight sandstone reservoirs, monoclinal folding may result in fracturing, which would increase the overall reservoir porosity and permeability. Despite these notes of caution, the results of the present study demonstrate an approach to understanding the effect of structural heterogeneity in contractional fault-propagation folds that is applicable to other settings if local factors such as significant diagenetic heterogeneities are taken into consideration.

It is also worth noting that deformation band permeabilities have to be in the lower range of what has been reported in the literature to significantly affect flow dynamics and production profiles (Fossen and Bale, 2007). Higher-permeability bands have a smaller effect on flow and can probably safely be disregarded if the contrast to host rock is only one–two orders of magnitude (see Figure 7, Table 5).

SUMMARY AND CONCLUSIONS

The present study has investigated the effect of structural heterogeneity (deformation bands) on simulated fluid flow across the limb of a contractional fold. A reservoir model of the study area in the San Rafael monocline was built, and following computation of upscaled grid cell permeabilities, six reservoir simulation models were run. The main conclusions drawn are summarized here.

- Deformation bands 1–2 orders of magnitude less permeable than their host rock had negligible effects only on simulated fluid flow and production performance.
- Deformation bands 3 orders of magnitude less permeable than their host rock had a limited effect on fluid flow and production performance.
- Deformation bands 4–5 orders of magnitude less permeable than their host rock had a significant effect on fluid flow and production performance, significantly delaying water breakthrough and prolonging production. This led to improved sweep efficiency in the lower-permeability models, yielding better production results in terms of total produced volumes and total recovery.
- Deformation band arrays have capabilities of redirecting flow regardless of amount of permeability contrast between them and the host rock; however, in terms of effect on large-scale production, the contrast needs to be at least 3 orders of magnitude to have a noticeable effect. Once the difference is at least 3 orders, our simulation shows a positive effect of sweeping efficiency as deformation bands become less permeable with respect to host rock, allowing for a higher fluid path tortuosity that resulted in less bypassed oil and ultimate higher recoveries. In any case, long-term production is needed to detect the effect of deformation bands in a comparable subsurface reservoir.
- When planning well placement and optimizing production strategies for oil and/or gas fields set in contractionally formed folds, geologists and engineers must take into consideration that significant strike-parallel, flow-impeding structural heterogeneity may exist. This must be incorporated in reservoir simulation models to more accurately plan and predict flow and production.

Note that the conclusions are based on simulations of two-phase flow where water is displacing oil; the effects of the deformation bands on flow for depletion-driven hydrocarbon production were not investigated in this study.

Auxiliary computational techniques such as the one presented in this study improve significantly the incorporation of small-scale features with strong scale gap into conventional sized reservoirs to upscale deformation features to be assessed at regional scale and whose geometry is not aligned with the general Cartesian orientation of the grid.

APPENDIX: DYNAMIC PROPERTIES OF FLOW SIMULATIONS

Table 6. Dynamic Properties of Flow Simulations

Parameter	Value
Length of run	50 yr
Report step	One quarter
Rock compressibility	0.0000435 bar^{-1}
Rock reference pressure	275.79 bars
Oil specific gravity	0.8
Saturation functions	
Corey exponents	Water = 4
	Oil–water = 3 (water wet to mixed wettability)
Saturation endpoints	Residual oil saturation to water, Sorw = 0.2
	Critical water saturation, Swcr = 0.2
Relative permeability endpoints	Maximum oil relative permeability, kromax(1 – Swcr) = 1
	Water relative permeability, krw(Sorw) = 0.4
Oil–water contact	800 masl
Reference depth and pressure	1800 masl; 181 bars
Gas/oil ratio	No gas
Wells	Three injectors
	Three producers
Flow rate	Injectors 100,000 Sm^3/day (~628,000 BWPD)
	Producers 90,000 Sm^3/day (~566,000 BOPD)
Bottom hole pressure (producers)	100 bars
Initial oil in place	5.7455×10^9 rm^3

Abbreviations: masl = meters above sea level; rm = reservoir cubic meters.

REFERENCES CITED

Antonellini, M., and A. Aydin, 1994, Effect of faulting on fluid flow in porous sandstones: Petrophysical properties: AAPG Bulletin, v. 78, no. 3, p. 355–377.

Antonellini, M., and A. Aydin, 1995, Effect of faulting on fluid flow in porous sandstones: Geometry and spatial distribution: AAPG Bulletin, v. 79, no. 5, p. 642–671.

Aydin, A., 1978, Small faults formed as deformation bands in sandstone: Pure and Applied Geophysics, v. 116, p. 913–930, doi:10.1007/BF00876546.

Ballas, G., H. Fossen, and R. Soliva, 2015, Factors controlling permeability of cataclastic deformation bands and faults in porous sandstone reservoirs: Journal of Structural Geology, v. 76, p. 1–21, doi:10.1016/j.jsg.2015.03.013.

Ballas, G., R. Soliva, J.-P. Sizun, A. Benedicto, T. Cavailhes, and S. Raynaud, 2012, The importance of the degree of cataclasis in shear bands for fluid flow in porous sandstone, Provence, France: AAPG Bulletin, v. 96, no. 11, p. 2167–2186, doi:10.1306/04051211097.

Beitler, B., M. A. Chan, and W. T. Parry, 2003, Bleaching of Jurassic Navajo Sandstone on Colorado Plateau Laramide highs: Evidence of exhumed hydrocarbon supergiants?: Geology, v. 31, no. 12, p. 1041–1044, doi:10.1130/G19794.1.

Biteau, J.-J., A. Le Marrec, M. Le Vot, and J.-M. Masset, 2006, The Aquitaine Basin: Petroleum Geoscience, v. 12, no. 3, p. 247–273, doi:10.1144/1354-079305-674.

Brandenburg, J. P., F. O. Alpak, J. G. Solum, and S. J. Naruk, 2012, A kinematic trishear model to predict deformation bands in a fault-propagation fold, East Kaibab monocline, Utah: AAPG Bulletin, v. 96, no. 1, p. 109–132, doi:10.1306/05101110160.

Bump, A. P., and G. H. Davis, 2003, Late Cretaceous–early Tertiary Laramide deformation of the northern Colorado Plateau, Utah and Colorado: Journal of Structural Geology, v. 25, no. 3, p. 421–440, doi:10.1016/S0191-8141(02)00033-0.

Corbett, P. W. M., and J. L. Jensen, 1993, Quantification of variability in laminated sediments: A role for the probe permeameter in improved reservoir characterization: Geological Society, London, Special Publications 1993, v. 73, no. 1, p. 433–442, doi:10.1144/GSL.SP.1993.073.01.25.

Crawford, B. R., 1998, Experimental fault sealing: Shear band permeability dependency on cataclastic fault gouge characteristics, *in* M. P. Coward, H. Johnson, and T. S. Daltaban, eds., Structural geology in reservoir

characterization: Geological Society, London, Special Publications 1998, v. 127, p. 83–97, doi:10.1144/GSL.SP.1998.127.01.04.

Davis, G. H., 1999, Structural geology of the Colorado Plateau Region of southern Utah, with special emphasis on deformation bands: Geological Society of America Special Paper 342, 157 p.

DeCelles, P. G., and J. C. Coogan, 2006, Regional structure and kinematic history of the Sevier fold-and-thrust belt, central Utah: Geological Society of America Bulletin, v. 118, p. 841–864, doi:10.1130/B25759.1.

Deng, S., L. Zuo, A. Aydin, J. Dvorkin, and T. Mukerji, 2015, Permeability characterization of natural compaction bands using core flooding experiments and three-dimensional image-based analysis: Comparing and contrasting the results from two different methods: AAPG Bulletin, v. 99, no. 1, p. 27–49, doi:10.1306/07071413211.

Dickinson, W., and W. Snyder, 1978, Plate tectonics of the Laramide orogeny: Geological Society of America Memoirs, v. 151, p. 355–366, doi:10.1130/MEM151-p355.

Doelling, H. H., 2002, Interim geologic map of the San Rafael Desert 30 x 60 quadrangle Emery and Grand Counties, Utah: Utah Geological Survey Open-File Report 404, scale 1:100,000, 22 sheets.

Durlofsky, L. J., 2003, Upscaling of geocellular models for reservoir flow simulation: A review of recent progress: 7th International Forum on Reservoir Simulation, Bühl/Baden-Baden, Germany, June 23–27, 2003, 58 p.

Eichhubl, P., W. L. Taylor, D. D. Pollard, and A. Aydin, 2004, Paleo-fluid flow and deformation in the Aztec Sandstone at the Valley of Fire, Nevada–Evidence for the coupling of hydrogeologic, diagenetic, and tectonic processes: Geological Society of America Bulletin, v. 116, no. 9, p. 1120–1136, doi:10.1130/B25446.1.

Fischer, M. P., and R. D. Christensen, 2004, Insights into the growth of basement uplifts deduced from a study of fracture systems in the San Rafael monocline, east central Utah: Tectonics, v. 23, no. 1, TC1018, 14 p., doi:10.1029/2002TC001470.

Fisher, Q. J., and R. J. Knipe, 2001, The permeability of faults within siliciclastic petroleum reservoirs of the North Sea and Norwegian Continental Shelf: Marine and Petroleum Geology, v. 18, p. 1063–1081, doi:10.1016/S0264-8172(01)00042-3.

Fossen, H., and A. Bale, 2007, Deformation bands and their influence on fluid flow: AAPG Bulletin, v. 91, no. 12, p. 1685–1700, doi:10.1306/07300706146.

Fossen, H., R. A. Schultz, Z. K. Shipton, and K. Mair, 2007, Deformation bands in sandstone: A review: Journal of the Geological Society, v. 164, p. 755–769, doi:10.1144/0016-76492006-036.

Fossen, H., L. F. Zuluaga, G. Ballas, R. Soliva, and A. Rotevatn, 2015, Contractional deformation of porous sandstone: Insights from the Aztec Sandstone, SE Nevada, USA: Journal of Structural Geology, v. 74, p. 172–184, doi:10.1016/j.jsg.2015.02.014.

Freeman, D. H., 1990, Permeability effects of deformation bands in porous sandstones, master's thesis, University of Oklahoma, Norman, Oklahoma, 90 p.

Gabrielsen, R. H., R. Aarland, and E. Alsaker, 1998, Identification and spatial distribution of fractures in porous, siliclastic sediments, *in* M. P. Coward, H. Johnson, and T. S. Daltaban, eds., Structural geology in reservoir characterization: Geological Society, London, Special Publications 1998, v. 127, p. 49–64, doi:10.1144/GSL.SP.1998.127.01.05.

Hintze, L. F., 1988, Geologic history of Utah: Provo, Utah, Brigham Young University, Geology Studies Special Publication 7, 202 p.

Jackson, J., K. Priestley, M. Allen, and M. Berberian, 2002, Active tectonics of the south Caspian basin: Geophysical Journal International, v. 148, no. 2, p. 214–245.

Jackson, M., and A. Muggeridge, 2000, Effect of discontinuous shales on reservoir performance during horizontal waterflooding: SPE Journal, v. 5, no. 4, p. 446–455, doi:10.2118/69751-PA.

Jamison, W. R., and D. W. Stearns, 1982, Tectonic deformation of Wingate Sandstone, Colorado National Monument: AAPG Bulletin, v. 66, no. 12, p. 2584–2608.

Karimi-Fard, M., L. Durlofsky, and K. Aziz, 2003, An efficient discrete fracture model applicable for general purpose reservoir simulators: SPE Reservoir Simulation Symposium, Houston, Texas, February 3–5, 2003, SPE-79699-MS, 11 p., doi:10.2118/79699-MS.

Knipe, R. J., Q. J. Fisher, M. R. Clennell, A. B. Farmer, A. Harrison, B. Kidd, E. McAllister, J. R. Porter, and E. A. White, 1997, Fault seal analysis: Successful methodologies, application and future directions, *in* P. Møller-Pedersen and A. G. Koestler, eds., Hydrocarbon seals: Importance for exploration and production: Norwegian Petroleum Society Special Publication 7 p. 15–38, doi:10.1016/S0928-8937(97)80004-5.

Lewis, H., and G. D. Couples, 1993, Production evidence for geological heterogeneities in the Anschutz Ranch East field, western USA: Geological Society, London, Special Publications 1993, v. 73, p. 321–338, doi:10.1144/GSL.SP.1993.073.01.19.

Marshak, S., K. Karlstrom, and J. M. Timmons, 2000, Inversion of Proterozoic extensional faults: An explanation for the pattern of Laramide and Ancestral Rockies intracratonic deformation, United States: Geology, v. 28, no. 8, p. 735–738, doi:10.1130/0091-7613(2000)28<735:IOPEFA>2.0.CO;2.

Matthäi, S. K., A. Aydin, D. D. Pollard, and S. G. Roberts, 1998, Numerical simulation of departures from radial drawdown in a faulted sandstone reservoir with joints and deformation bands: Geological Society, London, Special Publications 1998, v. 147, p. 157–191, doi:10.1144/GSL.SP.1998.147.01.11.

McQuarrie, N., 2004, Crustal scale geometry of the Zagros fold–thrust belt, Iran: Journal of Structural Geology, v. 26, no. 3, p. 519–535, doi:10.1016/j.jsg.2003.08.009.

Menéndez, B., W. Zhu, and T.-F. Wong, 1996, Micromechanics of brittle faulting and cataclastic flow in Berea sandstone: Journal of Structural Geology, v. 18, p. 1–16, doi:10.1016/0191-8141(95)00076-P.

Mitra, S., 1990, Fault-propagation folds: Geometry, kinematic evolution, and hydrocarbon traps: AAPG Bulletin, v. 74, no. 6, p. 921–945.

Parry, W. T., M. A. Chan, and B. P. Nash, 2009, Diagenetic characteristics of the Jurassic Navajo Sandstone in the Covenant oil field, central Utah thrust belt: AAPG Bulletin, v. 93, no. 8, p. 1039–1061, doi:10.1306/04270908170.

Pittman, E. D., 1981, Effect of fault-related granulation on porosity and permeability of quartz sandstones, Simpson Group (Ordovician), Oklahoma: AAPG Bulletin, v. 65, no. 11, p. 2381–2387.

Rotevatn, A., and H. Fossen, 2011, Simulating the effect of subseismic fault tails and process zones in a siliciclastic reservoir analogue: Implications for aquifer support and trap definition: Marine and Petroleum Geology, v. 28, no. 9, p. 1648–1662, doi:10.1016/j.marpetgeo.2011.07.005.

Rotevatn, A., H. Fossen, J. Hesthammer, T. E. Aas, and J. A. Howell, 2007, Are relay ramps conduits for fluid flow? Structural analysis of a relay ramp in Arches National Park, Utah, *in* L. Lonergan, R. J. H. Jolly, K. Rawnsley, and D. J. Sanderson, eds., Fractured reservoirs: Geological Society, London, Special Publications 2007, v. 270, p. 55–71, doi:10.1144/GSL.SP.2007.270.01.04.

Rotevatn, A., T. Sandve, E. Keilegavlen, D. Kolyukhin, and H. Fossen, 2013, Deformation bands and their impact on fluid flow in sandstone reservoirs: The role of natural thickness variations: Geofluids, v. 13, no. 3, p. 359–371, doi:10.1111/gfl.12030.

Rotevatn, A., J. Tveranger, J. A. Howell, and H. Fossen, 2009, Dynamic investigation of the effect of a relay ramp on simulated fluid flow: Geocellular modelling of the Delicate Arch Ramp, Utah: Petroleum Geoscience, v. 15, p. 45–58, doi:10.1144/1354-079309-779.

Sandve, T., I. Berre, and J. M. Nordbotten, 2012, An efficient multi-point flux approximation method for discrete fracture–matrix simulations: Journal of Computational Physics, v. 231, no. 9, p. 3784–3800, doi:10.1016/j.jcp.2012.01.023.

Schueller, S., A. Braathen, H. Fossen, and J. Tveranger, 2013, Spatial distribution of deformation bands in damage zones of extensional faults in porous sandstones: Statistical analysis of field data: Journal of Structural Geology, v. 52, p. 148–162, doi:10.1016/j.jsg.2013.03.013.

Shipton, Z. K., J. P. Evans, K. Robeson, C. B. Forster, and S. Snelgrove, 2002, Structural heterogeneity and permeability in faulted aeolian sandstone: Implications for subsurface modelling of faults: AAPG Bulletin, v. 86, no. 5, p. 863–883.

Soliva, R., R. A. Schultz, G. Ballas, A. Taboada, C. Wibberley, E. Saillet, and A. Benedicto, 2013, A model of strain localization in porous sandstone as a function of tectonic setting, burial and material properties; new insight from Provence (southern France): Journal of Structural Geology, v. 49, p. 50–63, doi:10.1016/j.jsg.2012.11.011.

Solum, J. G., J. P. Brandenburg, S. J. Naruk, O. V. Kostenko, S. J. Wilkins, and R. A. Schultz, 2010, Characterization of deformation bands associated with normal and reverse stress states in the Navajo Sandstone, Utah: AAPG Bulletin, v. 94, no. 9, p. 1453–1475, doi:10.1306/01051009137.

Sternlof, K. R., J. R. Chapin, D. D. Pollard, and L. J. Durlofsky, 2004, Permeability effects of deformation band arrays in sandstone: AAPG Bulletin, v. 88, no. 9, p. 1315–1329, doi:10.1306/032804.

Sternlof, K., M. Karimi-Fard, and L. J. Durlofsky, 2006, Flow and transport effects of compaction bands in sandstone at scales relevant to aquifer and reservoir management: Water Resources Research, v. 42, W07425, 16 p., doi:10.1029/2005WR004664.

Taylor, W. L., and D. D. Pollard, 2000, Estimation of in situ permeability of deformation bands in porous sandstone, Valley of Fire, Nevada: Water Resources Research, v. 36, no. 9, p. 2595–2606, doi:10.1029/2000WR900120.

Tindall, S. E., and G. H. Davis, 1999, Monocline development by oblique-slip fault-propagation folding: The East Kaibab monocline, Colorado Plateau, Utah: Journal of Structural Geology, v. 21, p. 1303–1320, doi:10.1016/S0191-8141(99)00089-9.

Torabi, A., and H. Fossen, 2009, Spatial variation of microstructure and petrophysical properties along deformation bands in reservoir sandstones: AAPG Bulletin, v. 93, no. 7, p. 919–938, doi:10.1306/03270908161.

Torabi, A., H. Fossen, and B. Alaei, 2008, Application of spatial correlation functions in permeability estimation of deformation bands in porous rocks: Journal of Geophysical Research, v. 113, B08208, 10 p., doi:10.1029/2007JB005455.

Zuluaga, L. F., H. Fossen, and A. Rotevatn, 2014, Progressive evolution of deformation band populations during Laramide fault-propagation folding: Navajo Sandstone, San Rafael monocline, Utah, U.S.A.: Journal of Structural Geology, v. 68, Part A, p. 66–81, doi:10.1016/j.jsg.2014.09.008.